ARTICLE   **Open Access**

Efficient X-ray luminescence imaging with ultrastable and eco-friendly copper(I)-iodide cluster microcubes

Yanze Wang[1], Wenjing Zhao[1], Yuanyuan Guo[1], Wenbo Hu [1], Chenxi Peng[1], Lei Li[1,2], Yuan Wei[1], Zhongbin Wu[1], Weidong Xu [1], Xiyan Li [3], Yung Doug Suh [4], Xiaowang Liu [1✉] and Wei Huang [1,5,6✉]

Abstract

The advancement of contemporary X-ray imaging heavily depends on discovering scintillators that possess high sensitivity, robust stability, low toxicity, and a uniform size distribution. Despite significant progress in this field, the discovery of a material that satisfies all of these criteria remains a challenge. In this study, we report the synthesis of monodisperse copper(I)-iodide cluster microcubes as a new class of X-ray scintillators. The as-prepared microcubes exhibit remarkable sensitivity to X-rays and exceptional stability under moisture and X-ray exposure. The uniform size distribution and high scintillation performance of the copper(I)-iodide cluster microcubes make them suitable for the fabrication of large-area, flexible scintillating films for X-ray imaging applications in both static and dynamic settings.

Introduction

Scintillators are optical materials that emit low-energy ultraviolet and visible photons in response to ionizing radiation such as X-rays and gamma rays[1-7]. This property makes scintillating materials useful for applications like nondestructive testing, X-ray astronomy, security inspection, and medical imaging[8-11]. Traditional inorganic scintillators that contain heavy metals usually have excellent performance, but their high-temperature requirement for bulk crystal growth hampers their use in the development of large-area and flexible X-ray detectors[12-15]. Additionally, many commercially available scintillators like CsI:Tl and LaBr$_3$:Ce are hygroscopic, adding difficulty to device fabrication. Recent developments in metal halide nanocrystals, such as CsPbBr$_3$ and Cs$_4$PbBr$_6$, show promise as a new class of scintillators with improved performance that can be processed in solution[16-20]. These features enable the fabrication of high-efficiency flexible X-ray imaging devices based on nanoscintillator-doped plastic substrates[21-23]. However, the challenge remains to develop efficient nano- and micro-scintillators with uniform morphology, environmentally-friendly composition, robust chemical stability, and integration into a stretchable substrate for flexible X-ray detectors[24-26].

To tackle the challenges outlined above, two key factors must be addressed. The first is to increase both the X-ray absorption ability and conversion efficiency of high-energy X-rays into low-energy photons in a scintillating material[27-30]. The second is to control the crystal growth process to produce homogeneous, small scintillators that are easy to use in flexible scintillation films[31]. Inspiration comes from the structure of a Cu(I)-I cluster, which is made up of a heavy inorganic core and organic ligands[32]. The idea is to create high-performing, eco-friendly scintillators by assembling these building blocks into crystalline nanoscale and microscale crystals[33,34]. This is because the large effective atomic number of Cu(I)-I cluster

Correspondence: Xiaowang Liu (iamxwliu@nwpu.edu.cn) or
Wei Huang (iamwhuang@nwpu.edu.cn)
[1]Frontiers Science Centre for Flexible Electronics (FSCFE), MIIT Key Laboratory of Flexible Electronics (KLoFE), Shaanxi Key Laboratory of Flexible Electronics, Xi'an Key Laboratory of Flexible Electronics, Xi'an Key Laboratory of Biomedical Materials & Engineering, Xi'an Institute of Flexible Electronics, Institute of Flexible Electronics (IFE), Northwestern Polytechnical University, Xi'an 710072 Shaanxi, China
[2]Key Laboratory of Magnetic Materials Devices, Ningbo Institute of Materials Technology and Engineering, Chinese Academy of Sciences, Ningbo 315201, China
Full list of author information is available at the end of the article

compounds provides strong X-ray stopping power (Supplementary Eqs. (S1) and (S2)), and the exceptional X-ray conversion efficiency stems from their photoluminescence and semiconducting properties (Supplementary Eq. (S3))[35,36]. Additionally, structure engineering improves the lattice stability of Cu(I)-I cluster scintillators and makes them more resistant to moisture, making it possible to rationally grow the crystals through a wet chemical process.

In this report, we present the development of high-performance monodisperse microcube scintillators made of copper iodide-(1-propyl-1,4-diazabicyclo[2.2.2]octan-1-ium)$_2$ ($Cu_4I_6(pr\text{-}ted)_2$) using a hot-injection method followed by thermal annealing at 200 °C for 1.5 h under a nitrogen atmosphere. Our experiments show that the as-prepared $Cu_4I_6(pr\text{-}ted)_2$ microcubes exhibit strong green radioluminescence at 535 nm, which is identical to phosphorescence under 365 nm excitation, and enable a low X-ray detection limit of 22 nGy_{air} s^{-1}. Additionally, we demonstrate that these microcube scintillators are remarkably robust to both water and X-rays. Moreover, we showcase the attractive applications of the uniform $Cu_4I_6(pr\text{-}ted)_2$ microcubes as microfillers in the fabrication of flexible, high-performance composite scintillators for small animal X-ray imaging in both static and dynamic settings. Our results suggest that these microcubes hold great promise as advanced scintillator materials for radiation detection and imaging.
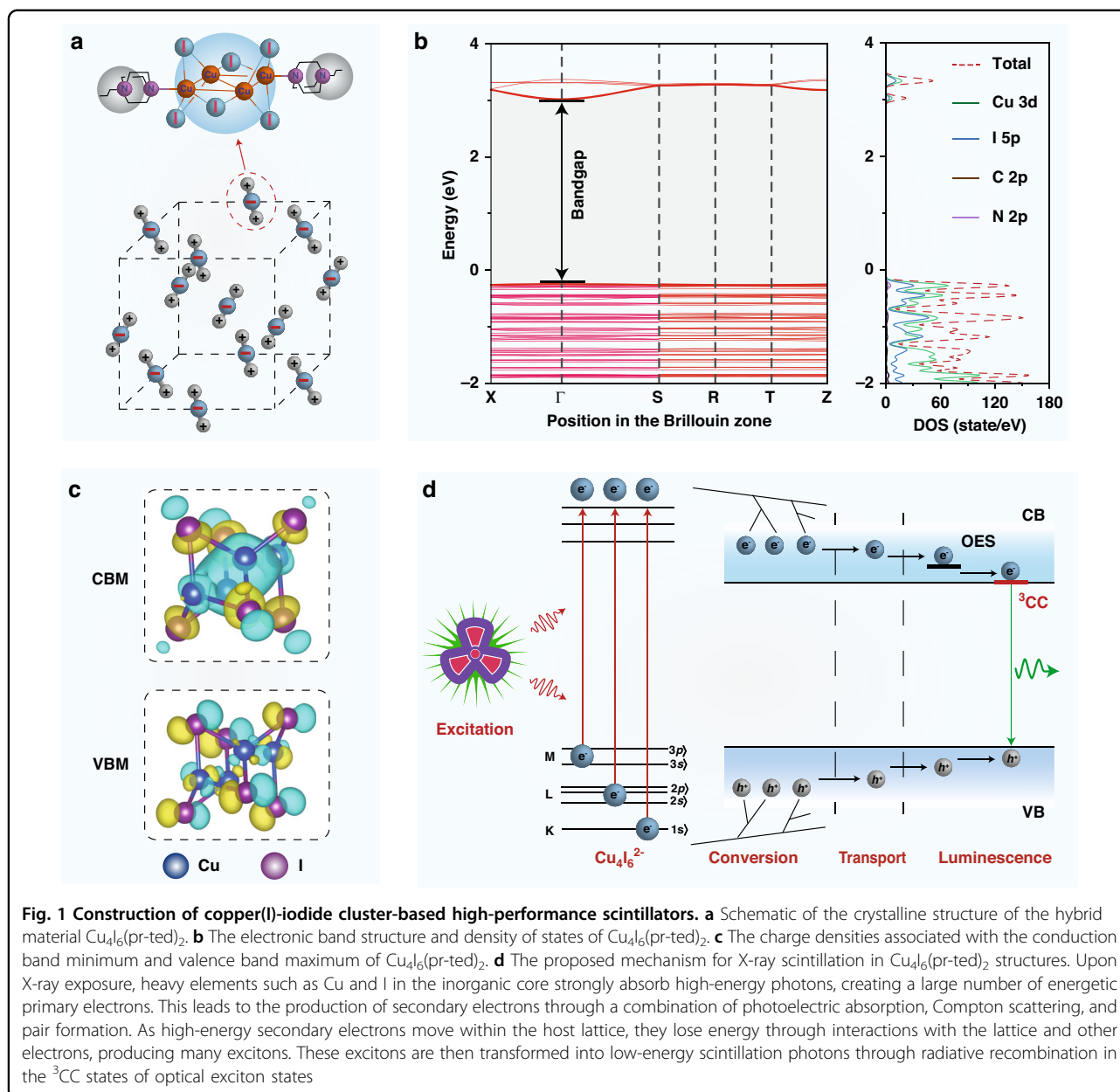
Results

To test our hypothesis, we selected $Cu_4I_6(pr\text{-}ted)_2$) in the orthorhombic crystal structure P222 as our model (Fig. 1a)[37]. We used density functional theory to study the electronic band structure of the inorganic-organic hybrid $Cu_4I_6(pr\text{-}ted)_2$ semiconductor. Our density functional theory (DFT) calculations showed a bandgap of 2.93 eV (Fig. 1b). The conduction band is mainly supported by Cu and I atomic orbitals, like Cu 3d and I 5p, as shown by the calculated conduction band minimum (CBM) and valence band maximum (VBM) (Fig. 1c). These results suggest that the $Cu_4I_6{}^{2-}$ core has high electronic delocalization, which leads to efficient energy migration from the host to the emission centers and strong emission from triplet cluster-centered (^{3}CC) excited states, as the excited energy converges from other excited states (OESs) (Supplementary Fig. S1)[38]. The combination of these intrinsic optical properties and the semiconducting nature of $Cu_4I_6(pr\text{-}ted)_2$ crystals results in high scintillation performance when exposed to X-ray irradiation (Fig. 1d).

The preparation of $Cu_4I_6(pr\text{-}ted)_2$ microcubes was carried out by injecting pr-ted into a mixture of KI-saturated CuI and polyvinylpyrrolidone (PVP) at 70 °C. The reaction was then quenched using a water-ice bath. X-ray diffraction (XRD) analysis confirmed the orthorhombic

phase of the $Cu_4I_6(pr\text{-}ted)_2$ microcubes, as supported by the match between the experimental and simulated XRD profiles (Supplementary Fig. S2). Scanning electron microscopy (SEM) revealed a uniform cubic morphology with an average size of 2.2 μm (Fig. 2a and Supplementary Fig. S3), with smooth and flat surfaces as observed under close inspection (Inset, Fig. 2a). Transmission electron microscopy also confirmed the cubic morphology of the $Cu_4I_6(pr\text{-}ted)_2$ microcrystals (Fig. 2b), and elemental mapping showed a homogeneous distribution of Cu, I, C, and N elements in selected microcrystals. These results were consistent with X-ray photoelectron spectroscopy, which confirmed the presence of Cu, I, C, and N in the microcubes (Supplementary Fig. S4). The Cu component was identified as Cu^+ based on the location of the Cu $2p_{3/2}$ peak at 929.1 eV[39]. The measured bandgap was 2.72 eV, which was slightly lower (0.21 eV) than the calculated value (Supplementary Fig. S5), likely due to delocalization error in the density functional approximations[40].
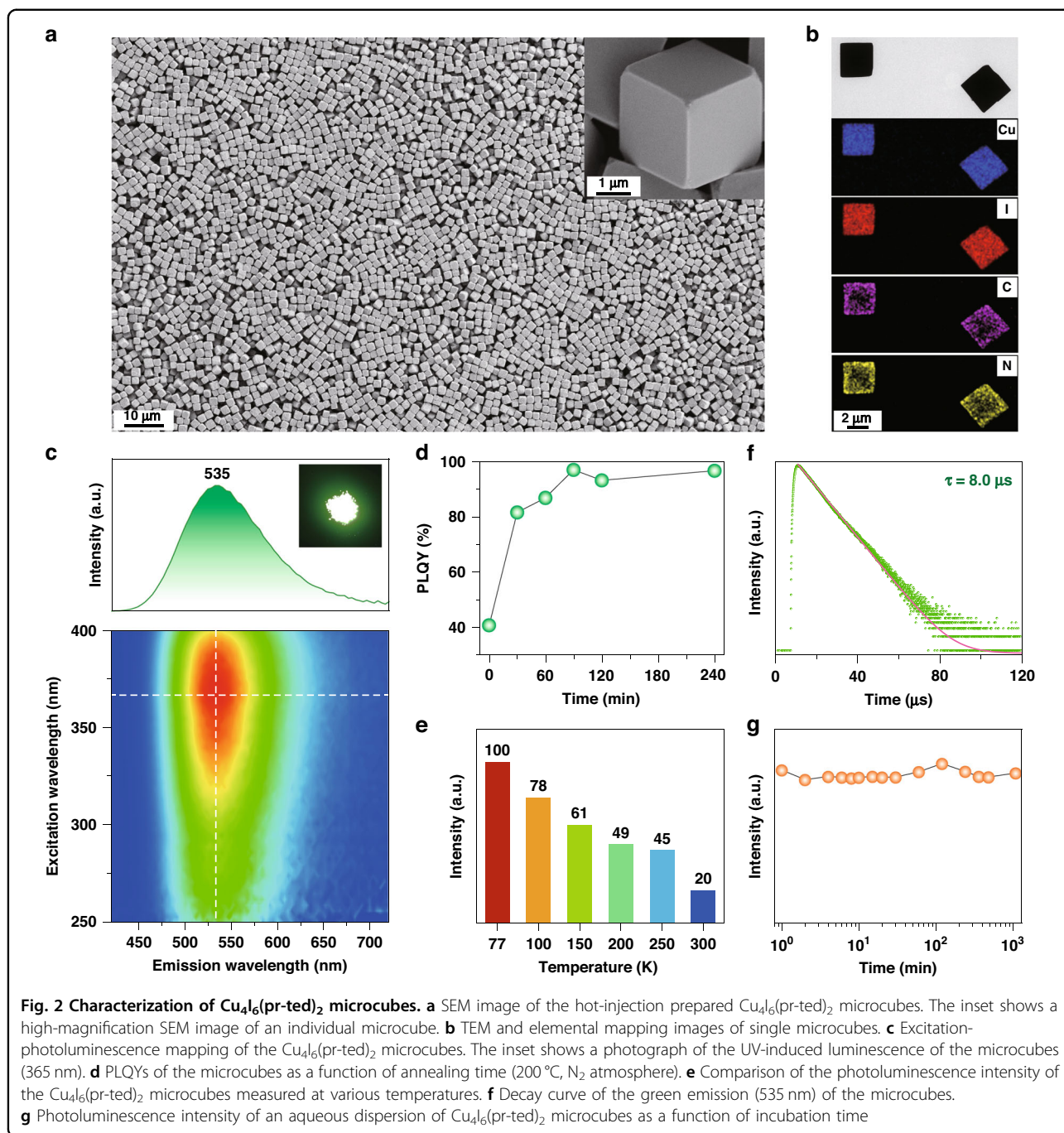
Next, we found that the formation of uniform $Cu_4I_6(pr\text{-}ted)_2$ microcubes requires precise control over nucleation kinetics. Traditional heating methods resulted in non-uniform spherical microparticles (Supplementary Fig. S6). Using room-temperature injection led to irregular $Cu_4I_6(pr\text{-}ted)_2$ particles, indicating that slow nucleation kinetics hinders the formation of uniform microcubes (Supplementary Fig. S7). At room temperature, the $Cu_4I_6(pr\text{-}ted)_2$ microcubes displayed a broad excitation band between 250–400 nm due to the inherent absorption of the building blocks[41]. Upon excitation at 370 nm, the microcubes showed maximum green emission at 535 nm (Fig. 2c) with a solid-state photoluminescence quantum yield (PLQY) of 40.7% (Supplementary Eq. (S4)). Annealing under a nitrogen atmosphere at 200 °C for different time periods (0.5, 1.0, and 1.5 h) increased the PLQY to 81.8%, 87.0%, and 97.1%, respectively (Fig. 2d). This annealing process significantly improved the crystallinity by reducing defect density in the $Cu_4I_6(pr\text{-}ted)_2$ microcubes (Supplementary Fig. S2), while having minimal impact on their cubic shape and size distribution (Supplementary Fig. S8). Note that our DFT calculations suggest the large possibility of the presence of Cu interstitials other than I interstitials and Cu and I vacancies because of their low formation energy of 0.58 eV. Moreover, the high thermal stability of $Cu_4I_6(pr\text{-}ted)_2$ microcubes in inert conditions was confirmed by the thermogravimetric analysis, which showed no apparent mass loss before 285 °C (Supplementary Fig. S9). These findings further support the attractiveness of $Cu_4I_6(pr\text{-}ted)_2$ microcubes as high-performance optical materials that can be treated at high temperatures for improving their luminescence performance.

In a further set of experiments, we evaluated the temperature-dependent optical properties of the

Fig. 1 Construction of copper(I)-iodide cluster-based high-performance scintillators. a Schematic of the crystalline structure of the hybrid material $Cu_4I_6(pr\text{-}ted)_2$. **b** The electronic band structure and density of states of $Cu_4I_6(pr\text{-}ted)_2$. **c** The charge densities associated with the conduction band minimum and valence band maximum of $Cu_4I_6(pr\text{-}ted)_2$. **d** The proposed mechanism for X-ray scintillation in $Cu_4I_6(pr\text{-}ted)_2$ structures. Upon X-ray exposure, heavy elements such as Cu and I in the inorganic core strongly absorb high-energy photons, creating a large number of energetic primary electrons. This leads to the production of secondary electrons through a combination of photoelectric absorption, Compton scattering, and pair formation. As high-energy secondary electrons move within the host lattice, they lose energy through interactions with the lattice and other electrons, producing many excitons. These excitons are then transformed into low-energy scintillation photons through radiative recombination in the ^3CC states of optical exciton states

synthesized $Cu_4I_6(pr\text{-}ted)_2$ microcubes. As the temperature decreased, we observed a narrowing of the emission profile, accompanied by a slight blue shift in the emission band (Supplementary Fig. S10). These observations were attributed to reduced structural torsion and an increased bandgap between the CBM and VBM of the $Cu_4I_6(pr\text{-}ted)_2$ microcubes at low temperatures. Additionally, the green emission improved due to a decrease in temperature-induced dissipation of vibrational energy (Fig. 2e). The lifetime of the green emission was measured at 8.0 μs at room temperature (Supplementary Eq. (S5) and Fig. 2f) and was found to increase at low temperatures (Supplementary Fig. S11). These optical results confirm that the green

emission originates from the ^3CC excited states with phosphorescence[42]. Notably, the $Cu_4I_6(pr\text{-}ted)_2$ microcubes showed remarkable resistance to degradation by water, as no noticeable changes in emission intensity were observed after 18 h of incubation in water (Fig. 2g). On the other hand, $CsPbBr_3$, $Cs_3Cu_2I_5$, and $CsCu_2I_3$ nano-/microparticles showed high susceptibility to moisture, with complete degradation of $CsPbBr_3$ and $Cs_3Cu_2I_5$ occurring within a few minutes with just a small amount of water (Supplementary Figs. S12 and S13). A increased resistance of $CsCu_2I_3$ micro-rods may be due to a combination of their large size and low Cu^+ solubility in the mixture (Supplementary Fig. S14)[43]. The improved water resistance

Fig. 2 Characterization of $Cu_4I_6(pr\text{-}ted)_2$ microcubes. a SEM image of the hot-injection prepared $Cu_4I_6(pr\text{-}ted)_2$ microcubes. The inset shows a high-magnification SEM image of an individual microcube. **b** TEM and elemental mapping images of single microcubes. **c** Excitation-photoluminescence mapping of the $Cu_4I_6(pr\text{-}ted)_2$ microcubes. The inset shows a photograph of the UV-induced luminescence of the microcubes (365 nm). **d** PLQYs of the microcubes as a function of annealing time (200 °C, N_2 atmosphere). **e** Comparison of the photoluminescence intensity of the $Cu_4I_6(pr\text{-}ted)_2$ microcubes measured at various temperatures. **f** Decay curve of the green emission (535 nm) of the microcubes. **g** Photoluminescence intensity of an aqueous dispersion of $Cu_4I_6(pr\text{-}ted)_2$ microcubes as a function of incubation time

of our $Cu_4I_6(pr\text{-}ted)_2$ microcubes is likely to be achieved by introducing coordination bonding between Cu and I, and between Cu and organic ligand, as opposed to the ionic nature of conventional scintillation materials. These findings indicate that it is possible to synthesize uniform micro-sized crystalline structures with exceptional luminescence and structural robustness by utilizing Cu(I)-I cluster building blocks.

The solid-state radioluminescence of $Cu_4I_6(pr\text{-}ted)_2$ microcubes was investigated at room temperature. The calculated effective atomic number of $Cu_4I_6(pr\text{-}ted)_2$ was 45.6, which is comparable to the X-ray absorption abilities of other materials such as $CsPbBr_3$, $Cs_3Cu_2I_5$, and $CsCu_2I_3$ (Fig. 3a and Supplementary Table S1)[44–46]. The $Cu_4I_6(pr\text{-}ted)_2$ microcubes exhibited strong single-band green radioluminescence at 535 nm upon X-ray excitation at a dose rate of 278 $\mu Gy_{air}\ s^{-1}$ (Fig. 3b and inset). The observed radioluminescence was found to be consistent with the photoluminescence, suggesting a common origin from the ^3CC excited states. These findings affirm the

Fig. 3 Radioluminescence characterization of $Cu_4I_6(pr-ted)_2$ microcubes. a Comparison of the X-ray absorption profile of $Cu_4I_6(pr-ted)_2$ and other reported scintillators. **b** Radioluminescence spectrum of $Cu_4I_6(pr-ted)_2$ microcubes at an excitation dose of 278 μGy_{air} s^{-1}. Inset: photograph of the radioluminescence image of the microcubes. **c** Radioluminescence comparison of $Cu_4I_6(pr-ted)_2$ microcubes with other reported or commercially available scintillators under the same excitation conditions. **d** Photocurrent curve for a $Cu_4I_6(pr-ted)_2$ microcube film with and without X-ray irradiation. Note that measurements were performed at different voltages. **e** Radioluminescence intensity of $Cu_4I_6(pr-ted)_2$ microcubes as a function of excitation dose. Note that a *DL* of 22 nGy_{air} s^{-1} is obtained via the 3σ/slope method. **f** X-ray tolerance of $Cu_4I_6(pr-ted)_2$ microcubes against continuous X-ray irradiation (dose rate: 2.85 mGy_{air} s^{-1}; top) and repeated X-ray irradiation (dose rate: 1.39 mGy_{air} s^{-1}, with an interval of 30 s, bottom). Note that the radioluminescence at 535 nm was monitored to check the robustness of $Cu_4I_6(pr-ted)_2$ microcubes

mechanism responsible for the strong radioluminescence displayed in Fig. 1d. The high-energy X-rays used in the experiment led to the ejection of numerous energetic primary electrons from the inner shells of both Cu and I atoms, along with the creation of holes. These primary electrons generated secondary electrons through kinetic energy dissipation during transport, resulting in the formation of a significant number of excitons in various excited states. These excitons were then converted to low-energy ^3CC excited states, which produced efficient radioluminescence through radiative recombination.

The sensitivity of $Cu_4I_6(pr-ted)_2$ microcubes to X-ray excitation was quantitatively compared with several commercially available or reported scintillators using the same dose rate of X-rays (Fig. 3c, Supplementary Fig. S15,

and Supplementary Table S2). We also fixed the size of our scintillation film to match that of conventionally available scintillation single crystals, with both having the same diameter (1.0 cm) and thickness (1.0 mm). Results showed that a thin film of the $Cu_4I_6(pr-ted)_2$ microcubes delivered radioluminescence that was 1.21, 3.41, and 36.36 times stronger than a single crystal of $YAlO_3$:Ce, $Bi_4Ge_3O_{12}$, and $PbWO_4$, respectively. In comparison to corresponding micro-/nano-particle films of $Cs_3Cu_2I_5$, $CsCu_2I_3$, and $CsPbBr_3$ under the same excitation conditions, the radioluminescence of $Cu_4I_6(pr-ted)_2$ microcubes was also 1.58, 3.56, and 9.90 times stronger, respectively. These observations support the hypothesis that $Cu_4I_6(pr-ted)_2$ microcubes exhibit not only remarkable X-ray stopping power but also high energy

conversion performance. The conductivity of a film of $Cu_4I_6(pr\text{-}ted)_2$ microcubes in the dark was also considerable, indicating their semiconducting nature and the feasibility of high-efficiency energy migration from the host to the emission centers, resulting in strong scintillation emissions (Fig. 3d and Supplementary Fig. S16). The photoconductive gain testing curve showed a higher current output upon X-ray irradiation at a dose rate of $3.4\,mGy_{air}\,s^{-1}$, suggesting the conversion of X-rays to visible photons in $Cu_4I_6(pr\text{-}ted)_2$ microcubes occurs through the formation of X-ray-induced charge carriers. As a result, $Cu_4I_6(pr\text{-}ted)_2$ microcubes exhibited a low detection limit (*DL*) of $22\,nGy_{air}\,s^{-1}$ (Fig. 3e), which is approximately 250 times lower than the standard dose for medical X-ray examinations ($5.5\,\mu Gy_{air}\,s^{-1}$)[47]. Additionally, the high robustness of $Cu_4I_6(pr\text{-}ted)_2$ microcubes to X-ray irradiation was demonstrated, as no noticeable degradation was observed during both continuous irradiations for 3 h and 8 cycles ($2.85\,mGy_{air}\,s^{-1}$) and repeated X-ray irradiation at 30-second intervals for 114 on-off cycles ($1.39\,mGy_{air}\,s^{-1}$).

The strong radioluminescence emission of $Cu_4I_6(pr\text{-}ted)_2$ microcubes in response to X-rays allows for the development of a flexible energy-conversion substrate for X-ray imaging. A large-sized polydimethylsiloxane (PDMS) film (169 cm^2, 0.5 mm thick) was fabricated by doping with 5.0 wt% of $Cu_4I_6(pr\text{-}ted)_2$ microcubes. The doped PDMS film demonstrated excellent flexibility, significant transparency, and emitted homogeneous and intense green radioluminescence upon X-ray excitation (Supplementary Fig. S17). These results suggest that the $Cu_4I_6(pr\text{-}ted)_2$ microcubes maintain their exceptional scintillation properties even after doping into the PDMS film. In addition, we found that doping $Cu_4I_6(pr\text{-}ted)_2$ microcubes at 5 wt% slightly increased the mechanical properties of the PDMS film, as evidenced by an increase in Young's modulus from 0.37 to 0.78 MPs (Supplementary Fig. S18). The enhanced mechanical strength can be attributed to the homogeneous distribution of the microcubes that have strong interactions with the PDMS matrix.

X-ray imaging was performed using a homemade setup (Fig. 4a) and resulted in a clear visualization of the detailed structure of a timer-printed circuit board (Fig. 4b and Supplementary Fig. S19). The imaging produced a full width at half maximum (FWHM) of 270 μm (Fig. 4c) and a resolution of 20.00 line pairs per millimeter (Fig. 4d). Conversely, using irregular $Cu_4I_6(pr\text{-}ted)_2$ microparticles as scintillating dopants resulted in aggregates in the plastic film surface, leading to defects in the X-ray images (Supplementary Fig. S20). Note that the resolution decreased to 3.5 lp/mm when increasing the thickness of the scintillating film to 1.0 mm as a result of an increased scattering effect (Supplementary Fig. S21). In addition, we found that the X-ray imaging performance of our
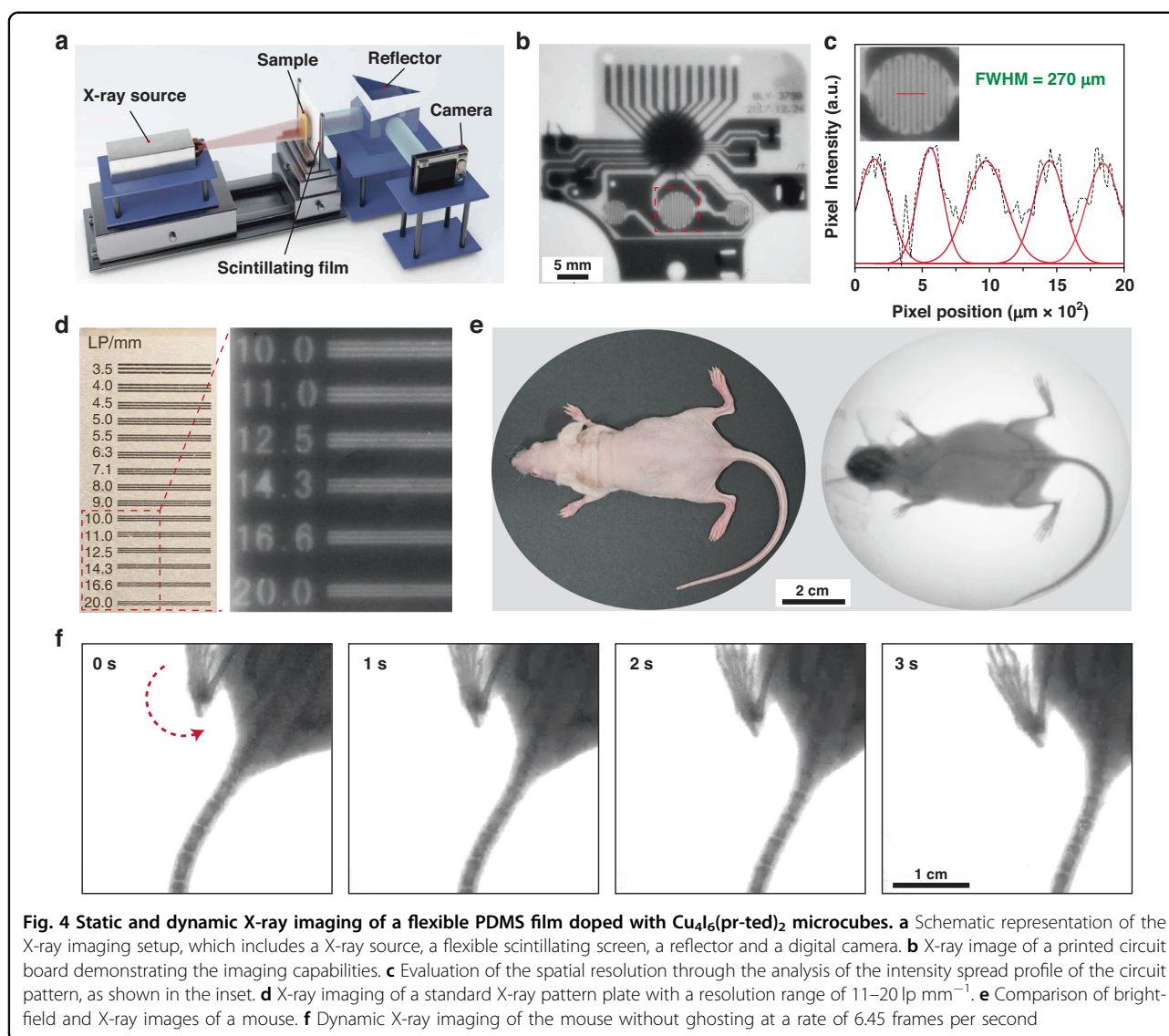
scintillation film did not deteriorate even after 2000 cycles of cyclic bending, suggesting that our scintillation film has a high anti-fatigue property (Supplementary Fig. S22). X-ray imaging of a nude mouse was also performed using the $Cu_4I_6(pr\text{-}ted)_2$ microcube-doped flexible screen and produced a clear image of the entire mouse skeleton (Fig. 4e), especially the tailbone where spacings between individual bones are clearly visible at about 226 μm (Supplementary Fig. S23). The radioluminescence of the as-prepared $Cu_4I_6(pr\text{-}ted)_2$ microcubes rapidly decreases to background levels (within 10 ms) after cessation of X-ray excitation (Supplementary Fig. S24), making the doped PDMS film particularly suitable for real-time dynamic X-ray imaging with no ghosting effect observed at an imaging rate of 6.45 frames per second (Fig. 4f, Supplementary Fig. S25, and Supplementary Movie S1)[48].

Discussion

In this study, we report on the potential of Cu(I)-I cluster structures as a new class of highly stable and eco-friendly scintillators due to their composition and optical characteristics. The high scintillation performance of the as-prepared $Cu_4I_6(pr\text{-}ted)_2$ microcubes allows for a low X-ray detection limit of $22\,nGy_{air}\,s^{-1}$. With the abundant choice of inorganic cores available, the X-ray absorption capability of Cu(I)-I cluster crystals can be further improved by introducing more I atoms while maintaining the high efficiency of converting X-rays into low-energy photons. Moreover, modulating the organic ligand shows promise in tuning the excited-state transitions in Cu(I)-I cluster crystals, enabling feasible color tuning of radioluminescence in the visible region.

A particularly attractive aspect of our work is that monodisperse $Cu_4I_6(pr\text{-}ted)_2$ microcubes can be produced using a kinetically controlled synthesis method, making them ideal for use as micro-sized scintillators in the development of large-scale and flexible scintillation screens for both static and dynamic X-ray imaging. Compared with conventional metal halide scintillation materials, $Cu_4I_6(pr\text{-}ted)_2$ microcubes exhibit excellent chemical stability. This feature not only provides considerable benefits in practical device manufacturing but also offers the potential to regulate the morphology and dimensions of Cu(I)-I cluster nanoscintillators to enhance their scintillation performance. For example, doping $Cu_4I_6(pr\text{-}ted)_2$ microcubes into a polymer matrix allows for the fabrication of plastic scintillating screens for flexible X-ray detection and imaging.

Overall, our results indicate that $Cu_4I_6(pr\text{-}ted)_2$ microcubes possess significant practical advantages, including enhanced chemical and optical stability, waterproofing, and low toxicity. These findings should stimulate further study on Cu(I)-I cluster materials to explore next-generation scintillators for innovative radiography.

Fig. 4 Static and dynamic X-ray imaging of a flexible PDMS film doped with Cu$_4$I$_6$(pr-ted)$_2$ microcubes. a Schematic representation of the X-ray imaging setup, which includes a X-ray source, a flexible scintillating screen, a reflector and a digital camera. **b** X-ray image of a printed circuit board demonstrating the imaging capabilities. **c** Evaluation of the spatial resolution through the analysis of the intensity spread profile of the circuit pattern, as shown in the inset. **d** X-ray imaging of a standard X-ray pattern plate with a resolution range of 11–20 lp mm^{-1}. **e** Comparison of bright-field and X-ray images of a mouse. **f** Dynamic X-ray imaging of the mouse without ghosting at a rate of 6.45 frames per second

Methods

Synthesis of pr-ted

The synthesis of pr-ted was conducted using a modified version of a previously reported method[41]. To synthesize pr-ted, 1-bromopropane (10 mmol) was dropped into a 50 mL acetone solution of triethylenediamine (Ted, 0.2 M) under magnetic stirring, forming a clear solution. This solution was then left at room temperature for 12 h, yielding a colorless oily product. The product was recovered by centrifugation, washed with ethyl acetate, and dried under vacuum. The final yield was estimated to be 68 wt%.

Synthesis of Cu$_4$I$_6$(pr-ted)$_2$ microcubes

In a typical experiment, PVP (K88-96, 0.02 g/mL, 12.5 mL) was dissolved in ethanol to form a solution, and a KI-saturated aqueous solution of CuI (0.5 mmol mL^{-1},

0.5 mL) was prepared. The two solutions were then mixed in a 50-mL flask at 70 °C while stirring with a magnet, resulting in a homogeneous pale yellow solution. An ethanol solution of pr-ted (0.5 mmol mL^{-1}, 0.5 mL) was then injected to the CuI-KI-PVP solution at 70 °C, and the mixture was immediately immersed in a water-ice bath. The final product, Cu$_4$I$_6$(pr-ted)$_2$ microcubes, was obtained through centrifugation at 6000 rpm for 5 min, followed by washing twice with deionized water and ethanol. The purified Cu$_4$I$_6$(pr-ted)$_2$ microcubes were then treated at 200 °C in a nitrogen atmosphere for different periods of time.

Synthesis of the flexible PDMS film doped with Cu$_4$I$_6$(pr-ted)$_2$ microcubes

In brief, treated Cu$_4$I$_6$(pr-ted)$_2$ microcubes (0.396 g) were mixed with a 1:1 solution of cyclohexane and

ethanol (10 mL) under sonication to form a homogeneous dispersion. This dispersion was then combined with a mixture of PDMS prepolymer (7.2 g) and curing agent (0.72 g) under vigorous stirring for 2 h. The mixture was then subjected to vacuum for 1 h to remove any volatile materials. The resulting gel-like substance was poured into a polytetrafluoroethylene mold ($13 \times 13 \, cm^2$) and cured at 200 °C for 1.5 h. The result was a flexible and transparent PDMS film doped with $Cu_4I_6(pr\text{-}ted)_2$ microcubes suitable for imaging applications.

Instrumentation

Scanning electron microscopy was performed using a Zeiss Gemini 300 microscope at a voltage of 3 kV. Transmission electron microscopy was conducted on a Hitachi HT 7700 operating at 120 kV. Powder X-ray diffraction characterization was carried out using a Bruker D8 Advance X-ray diffractometer with Cu Kα radiation. Photoluminescence emission profiles and decay curves were obtained using an FSL-1000 (Edinburgh Instruments Ltd.). PLQY measurements were performed on a C9920-02G system (Hamamatsu). Radioluminescence emission profiles were acquired using an Edinburgh FS5 fluorescence spectrophotometer (Edinburgh Instruments Ltd.), equipped with an external miniature X-ray source from AMPEK, Inc.

Author details
[1]Frontiers Science Centre for Flexible Electronics (FSCFE), MIIT Key Laboratory of Flexible Electronics (KLoFE), Shaanxi Key Laboratory of Flexible Electronics, Xi'an Key Laboratory of Flexible Electronics, Xi'an Key Laboratory of Biomedical Materials & Engineering, Xi'an Institute of Flexible Electronics, Institute of Flexible Electronics (IFE), Northwestern Polytechnical University, Xi'an 710072 Shaanxi, China. [2]Key Laboratory of Magnetic Materials Devices, Ningbo Institute of Materials Technology and Engineering, Chinese Academy of Sciences, Ningbo 315201, China. [3]Institute of Photoelectronic Thin Film Devices and Technology, Solar Energy Conversion Center, Nankai University, Tianjin 300350, China. [4]Department of Chemistry and School of Energy and Chemical Engineering, UNIST, Ulsan 44919, Korea. [5]State Key Laboratory of Organic Electronics and Information Displays & Institute of Advanced Materials(IAM), Nanjing University of Posts & Telecommunications, 9 Wenyuan Road, Nanjing 210023, China. [6]Key Laboratory of Flexible Electronics (KLOFE), Institute of Advanced Materials (IAM), Nanjing Tech University (Nanjing Tech), 30 South Puzhu Road, Nanjing 211816, China

Author contributions
X.L. and W.H. conceived and supervised the project. Y.W., W.Z., and Y.G. designed the experiments. Y.W. and W.Z. carried out the optical measurements. Y.W. and C.P. performed the synthesis of $Cu_4I_6(pr\text{-}ted)_2$ microcubes. L.L. performed the calculation of the density state plot for $Cu_4I_6(pr\text{-}ted)_2$. Y.W. carried out the X-ray imaging studies. Y.W., Z.W., X.L., W.X. and Y.D.S. provided insightful discussion. X.L. wrote the manuscript with input

References
1. Büchele, P. et al. X-ray imaging with scintillator-sensitized hybrid organic photodetectors. *Nat. Photonics* **9**, 843–848 (2015).
2. Ou, X. Y. et al. High-resolution X-ray luminescence extension imaging. *Nature* **590**, 410–415 (2021).
3. Ma, W. B. et al. Thermally activated delayed fluorescence (TADF) organic molecules for efficient X-ray scintillation and imaging. *Nat. Mater.* **21**, 210–216 (2022).
4. Wei, H. T. & Huang, J. S. Halide lead perovskites for ionizing radiation detection. *Nat. Commun.* **10**, 1066 (2019).
5. Maddalena, F. et al. Inorganic, organic, and perovskite halides with nano-technology for high-light yield X- and γ-ray scintillators. *Crystals* **9**, 88 (2019).
6. Heo, J. H. et al. High-performance next-generation perovskite nanocrystal scintillator for nondestructive X-ray imaging. *Adv. Mater.* **30**, 1801743 (2018).
7. Wang, Y. X. et al. Emergence of uranium as a distinct metal center for building intrinsic X-ray scintillators. *Angew. Chem. Int. Ed.* **57**, 7883–7887 (2018).
8. Spahn, M. et al. X-ray detectors in medical imaging. *Nucl. Instrum. Methods Phys. Res. Sect. A* **731**, 57–63 (2013).
9. Dujardin, C. et al. Needs, trends, and advances in inorganic scintillators. *IEEE Trans. Nucl. Sci.* **65**, 1977–1997 (2018).
10. Lecoq, P. Development of new scintillators for medical applications. *Nucl. Instrum. Methods Phys. Res. Sect. A* **809**, 130–139 (2016).
11. Wang, J. X. et al. Heavy-atom engineering of thermally activated delayed fluorophores for high-performance X-ray imaging scintillators. *Nat. Photonics* **16**, 869–875 (2022).
12. Zhao, J. J. et al. Perovskite-filled membranes for flexible and large-area direct-conversion X-ray detector arrays. *Nat. Photonics* **14**, 612–617 (2020).
13. Liu, J. Y. et al. Flexible, printable soft-X-Ray detectors based on all-inorganic perovskite quantum dots. *Adv. Mater.* **31**, 1901644 (2019).
14. van Breemen, A. J. J. M. et al. Curved digital X-ray detectors. *npj Flex. Electron.* **4**, 22 (2020).
15. Liang, Z. Y. et al. Thermoplastic membranes incorporating semiconductive metal–organic frameworks: an advance on flexible x-ray detectors. *Angew. Chem. Int. Ed.* **59**, 11856–11860 (2020).
16. Chen, Q. S. et al. All-inorganic perovskite nanocrystal scintillators. *Nature* **561**, 88–93 (2018).
17. Zhang, H. et al. Reproducible X-ray imaging with a perovskite nanocrystal scintillator embedded in a transparent amorphous network structure. *Adv. Mater.* **33**, 2102529 (2021).
18. Li, Y. et al. Lead-halide Cs_4PbBr_6 single crystals for high-sensitivity radiation detection. *NPG Asia Mater.* **13**, 40 (2021).
19. Cao, F. et al. Shining emitter in a stable host: design of halide perovskite scintillators for X-ray imaging from commercial concept. *ACS Nano* **14**, 5183–5193 (2020).
20. Zhang, Y. H. et al. Metal halide perovskite nanosheet for X-ray high-resolution scintillation imaging screens. *ACS Nano* **13**, 2520–2525 (2019).
21. Xu, L. J. et al. Highly efficient eco-friendly X-ray scintillators based on an organic manganese halide. *Nat. Commun.* **11**, 4329 (2020).
22. Hou, J. W. et al. Liquid-phase sintering of lead halide perovskites and metal-organic framework glasses. *Science* **374**, 621–625 (2021).
23. Gandini, M. et al. Efficient, fast and reabsorption-free perovskite nanocrystal-based sensitized plastic scintillators. *Nat. Nanotechnol.* **15**, 462–468 (2020).
24. Morad, V. et al. Disphenoidal zero-dimensional lead, tin, and germanium halides: highly emissive singlet and triplet self-trapped excitons and X-ray scintillation. *J. Am. Chem. Soc.* **141**, 9764–9768 (2019).

25. Zhang, M. Y. et al. Oriented-structured CsCu$_2$I$_3$ film by close-space sublimation and nanoscale seed screening for high-resolution X-ray imaging. *Nano Lett.* **21**, 1392–1399 (2021).

26. Zhu, W. J. et al. Low-dose real-time X-ray imaging with nontoxic double perovskite scintillators. *Light Sci. Appl.* **9**, 112 (2020).

27. Hajagos, T. J. et al. High-Z sensitized plastic scintillators: a review. *Adv. Mater.* **30**, 1706956 (2018).

28. Perego, J. et al. Composite fast scintillators based on high-*Z* fluorescent metal-organic framework nanocrystals. *Nat. Photonics* **15**, 393–400 (2021).

29. Pan, W. C. et al. Cs$_2$AgBiBr$_6$ single-crystal X-ray detectors with a low detection limit. *Nat. Photonics* **11**, 726–732 (2017).

30. Wu, H. D. et al. Metal halide perovskites for X-ray detection and imaging. *Matter* **4**, 144–163 (2021).

31. Yin, Y. D. & Alivisatos, A. P. Colloidal nanocrystal synthesis and the organic–inorganic interface. *Nature* **437**, 664–670 (2005).

32. Troyano, J., Zamora, F. & Delgado, S. Copper(I)-iodide cluster structures as functional and processable platform materials. *Chem. Soc. Rev.* **50**, 4606–4628 (2021).

33. Hei, X. Z. & Li, J. All-in-one: a new approach toward robust and solution-processable copper halide hybrid semiconductors by integrating covalent, coordinate and ionic bonds in their structures. *Chem. Sci.* **12**, 3805–3817 (2021).

34. Hei, X. Z. et al. Blending ionic and coordinate bonds in hybrid semiconductor materials: a general approach toward robust and solution-processable covalent/coordinate network structures. *J. Am. Chem. Soc.* **142**, 4242–4253 (2020).

35. Yanagida, T. Inorganic scintillating materials and scintillation detectors. *Proc. Jpn. Acad., Ser. B* **94**, 75–97 (2018).

36. Yanagida, T. et al. Fast and high light yield scintillation in the Ga$_2$O$_3$ semiconductor material. *Appl. Phys. Express* **9**, 042601 (2016).

37. Liu, W. et al. All-in-one: achieving robust, strongly luminescent and highly dispersible hybrid materials by combining ionic and coordinate bonds in molecular crystals. *J. Am. Chem. Soc.* **139**, 9281–9290 (2017).

38. Ford, P. C., Cariati, E. & Bourassa, J. Photoluminescence properties of multi-nuclear copper(I) compounds. *Chem. Rev.* **99**, 3625–3648 (1999).

39. Cohen, A. J., Mori-Sánchez, P. & Yang, W. T. Challenges for density functional theory. *Chem. Rev.* **112**, 289–320 (2012).

40. Li, M. H. et al. In-situ construction of novel naphthalenediimide/metal-iodide hybrid heterostructures for enhanced photoreduction of Cr (VI). *Dyes Pigments* **187**, 109146 (2021).

41. Wang, J. J. et al. Highly luminescent copper iodide cluster based inks with photoluminescence quantum efficiency exceeding 98%. *J. Am. Chem. Soc.* **142**, 3686–3690 (2020).

42. Xie, M. C. et al. Highly efficient sky blue electroluminescence from ligand-activated copper iodide clusters: overcoming the limitations of cluster light-emitting diode. *Sci. Adv.* **5**, eaav9857 (2019).

43. Cheng, P. F. et al. Colloidal synthesis and optical properties of all-inorganic low-dimensional cesium copper halide nanocrystals. *Angew. Chem. Int. Ed.* **58**, 16087–16091 (2019).

44. Berger, M. J. et al. *XCOM: Photon Cross Sections Database* (National Institute of Standards and Technology, 2013). https://www.nist.gov/pml/xcom-photon-cross-sections-database.

45. Cheng, S. L. et al. Zero-dimensional Cs$_3$Cu$_2$I$_5$ perovskite single crystal as sensitive X-ray and γ-ray scintillator. *Phys. Status Solidi* **14**, 2000374 (2020).

46. Cheng, S. L. et al. Non-hygroscopic, self-absorption free, and efficient 1D CsCu$_2$I$_3$ perovskite single crystal for radiation detection. *ACS Appl. Mater. Interfaces* **13**, 12198–12202 (2021).

47. Wei, H. T. et al. Sensitive X-ray detectors made of methylammonium lead tribromide perovskite single crystals. *Nat. Photonics* **10**, 333–339 (2016).

48. Hata, A. et al. Dynamic chest X-ray using a flat-panel detector system: technique and applications. *Korean J. Radiol.* **22**, 634–651 (2021).